MSE307 Engineering Alloys 2014-15 L7: Mechanical Behaviour of $\alpha + \beta$ Ti Alloys

D. Dye[a]

[a] *Rm G03b, Department of Materials, Imperial College London, London SW7 2AZ, UK. david.dye@imperial.ac.uk*

In this lecture we examine microstructure - property relationships and consider the mechanical behaviour of titanium alloys, and begin a discussion that will span into lecture 7 on fatigue behaviour.

We have said previously that in titanium alloys, the key is that on cooling from the β, there is little intragranular nucleation of α and so we see colonies of Widmanstätten α form. If we want a bimodal or equiaxed microstructure, we then deform these plates high in the $\alpha+\beta$ phase field, and then recrystallise them, also high in the $\alpha+\beta$ phase field. This isn't true recrystallisation where new grains nucleate and grow, rather it is the breakup and globularisation of the plates that already exist.

We've also looked and the α/β orientation relationship and habit plane, and concluded that there are 12 variants of α that can form from the β (6 distinct). Examining the habit plane, we further found that there was was was one prism slip system that could, relatively easily, be transmitted through an α/β colony structure, but that the other two easy slips would be restricted by the microstructure.

Turning to mechanical behaviour, we have already discussed the slip systems when we discussed the crystallography, with prism $<a>$ slip begin about 3× lower in CRSS that $<c+a>$ slip. The elastic modulus variation in α-Ti is shown in Figure 1. Thus, the (0002) c-axis direction is stiffest, whilst the prism plane normal - loading along a - is most compliant. Therefore in a polycrystal, grains with their (0002) along the loading direction will carry more of the load; in addition they are stronger. Therefore they are termed 'hard' grains. Therefore, as an hcp material, Ti is relatively isotropic, but its anisotropy still dominates the mechanical behaviour.

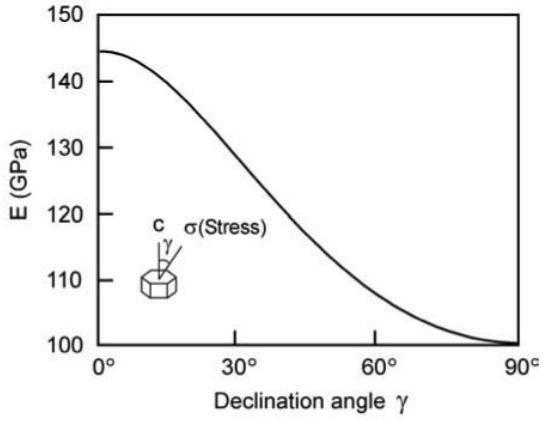

Figure 1: Variation in Young's modulus with declination from the c-axis for pure α-Ti single crystals. From Lütjering and Williams.

The β phase modulus varies with composition quite dramatically from 80-110 GPa, but is usually slightly lower than the α.

Any consideration of the mechanical behaviour, after considering the slip systems and elasticity, must then examine the overall stress-strain curves. Some curves for Ti-6Al-4V in equiaxed / bimodal forms, rolled to plate and bar, are shown in Figure 2. Ti-6Al-4V has a density of $4.43\,\mathrm{g\,cm^{-3}}$, a yield strength in the range of $\sigma_y = 850$-$1000\,\mathrm{MPa}$, a Young's modulus of about 110 GPa, ductility of $\sim$ 10% and $K_{1c} \approx 50\,\mathrm{MPa}\sqrt{\mathrm{m}}$. Compare these to a 300M landing great steel (Fe-0.4C-0.8Mn-1.6Si-0.8Cr-1.8Ni-0.4Mo-0.1V, wt.%), which is a quench+temper deep-hardenable steel with a yield strength $\sigma_y = 1.6\,\mathrm{GPa}$ and density of $4.43\,\mathrm{g\,cm^{-3}}$. Clearly titanium alloys are not much different in specific yield strength; the point is that their HCF strength is almost the same as the steel, but it is less than 60% of the density.

Examining the stress-strain curve, one thing is very noticeable - titanium alloys don't usually work harden much. This means that the maxima in the stress-strain curve arrives at relatively low stresses and so they become unstable

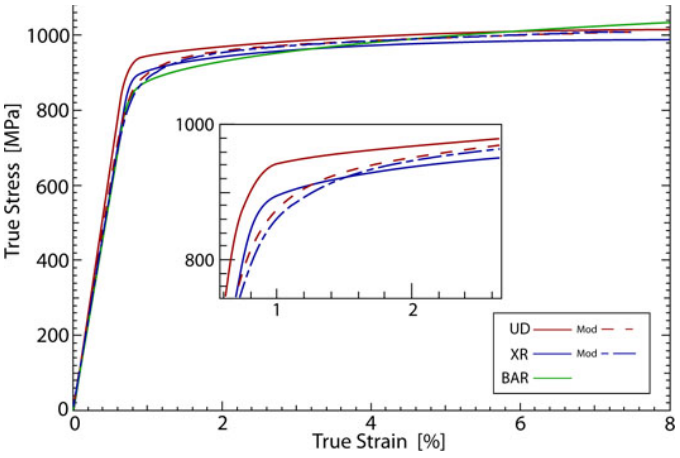

Figure 2: Variation in flow curve for three product forms of Ti-64 (UD and XR plate, and bar), along with curves from a micro mechanical model. From Warwick et al, Dye research grip, 2012.

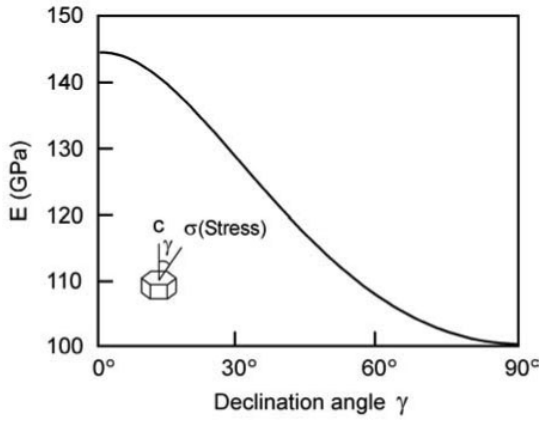

Figure 3: Effect of α grain size on HCF strength of fully equiaxed microstructures in Ti-6Al-4V, for fully reversed loading (R=-1). From Lütjering and Williams.

to small perturbations, and therefore fail in a ductile manner by necking. This also means that there is little work hardening at crack tips, which helps explain why titanium alloys' fatigue crack growth resistance isn't that amazing - once a crack is growing, it grows quite readily. The good fatigue performance of Ti is a result of a lack of initiating defects and good fatigue crack initiation resistance; and hence these alloys are described as 'notch sensitive.'

An S-N curve for Ti-64 is provided in Figure 3. Typical run-out HCF strengths for Ti alloys are around 550 MPa (for R=0); the Figure shows fully reversed loading and the effect of primary α grain size; it is observed that finer α_p sizes provide better HCF behaviour, as might be expected.

However, it is worth considering the fatigue crack growth behaviour; a da/dN - ΔK curve is provided in Figure 4. First take the Paris law $\frac{da}{dN} = C\Delta K^m$ where the stress intensity $\Delta K = y\sqrt{\pi a}$, a is the crack length, N the number of cycles, m and C are material constants and Y is a constant depending on the crack geometry. Then, apply it to this da/dN curve, assuming that the crack grows according to the Paris Law between threshold ΔK_{th} and fast fracture ΔK_{1c}. This gives C and m as shown on the graph.

Consider a scenario now where $\sigma_{\max} = 550\,\text{MPa}$, $\sigma_{\min} = 50\,\text{MPa}$ and $a_0 = 10\,\mu\text{m}$, with $Y = 0.7$. If we substitute for Δ_K in the Paris law, separate by parts and integrate, we obtain

$$N_f = \frac{-m}{C(Y\sqrt{\pi})^m}\Delta\sigma^{-m}\left[a^{(1-m/2)}\right]_{a_0}^{a_{K_{1c}}} \tag{1}$$

If we take $K_{1c} = 35\,\text{MPa}\sqrt{\text{m}}$ then we obtain $a = 2.63\,\text{mm}$. Substituting numbers gives

$$N_f = -1.688 \times 10^{13}\Delta\sigma^{-5.33}\left[a^{-1.66}\right]_{a_0}^{a_{K_{1c}}} \tag{2}$$

For this initial flaw size we therefore get

$$N_f = -1.688 \times 10^{13}\Delta\sigma^{-5.33}[19,200 - 199,500,000] \tag{3}$$

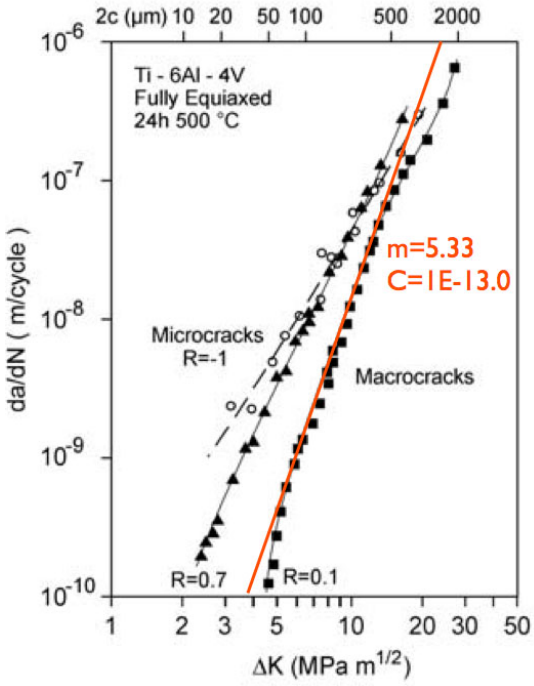

Figure 4: Ti-6Al-4V fatigue crack growth curve, overlaid with a Paris law fit for the fatigue crack growth regime.

and so the dependence on the stress for this initial microstructural flaw size is

$$N_f = 3.37 \times 10^{21}\Delta\sigma^{-5.33} \tag{4}$$

and in this case the life is

$$N_f = 13.8 \times 10^6 \text{cycles} \tag{5}$$

The only problem with this is that in this case the initial ΔK was $2.8\,\text{MPa}\sqrt{\text{m}}$, which is below the threshold ΔK_{th} measured experimentally - so this crack would actually last indefinitely without growing.

If you lack a ΔK_{th} measurement, you might try to estimate it from theory. But, the plastic zone size for a growing crack is given by

$$\frac{1}{6\pi}\left(\frac{K_{\max}}{\sigma_y}\right)^2 \tag{6}$$

If we substitute for the yield stress of 900 MPa and $\Delta K_{\text{th}} = 5\,\text{MPa}\sqrt{\text{m}}$, we obtain a plastic zone size at threshold of

$$\frac{1}{6\pi}\left(\frac{K_{\max}}{\sigma_y}\right)^2 = \frac{1}{6\pi}\left(\frac{5}{900}\right)^2 = 1.6\,\mu\text{m} \tag{7}$$

And so the plastic zone size is less than a typical primary α grain size, which suggests that at threshold we might be in trouble on microstructural ground. Actually, we are definitely in trouble here, because according to Kitigawa all of the continuum stress assumptions in linear elastic

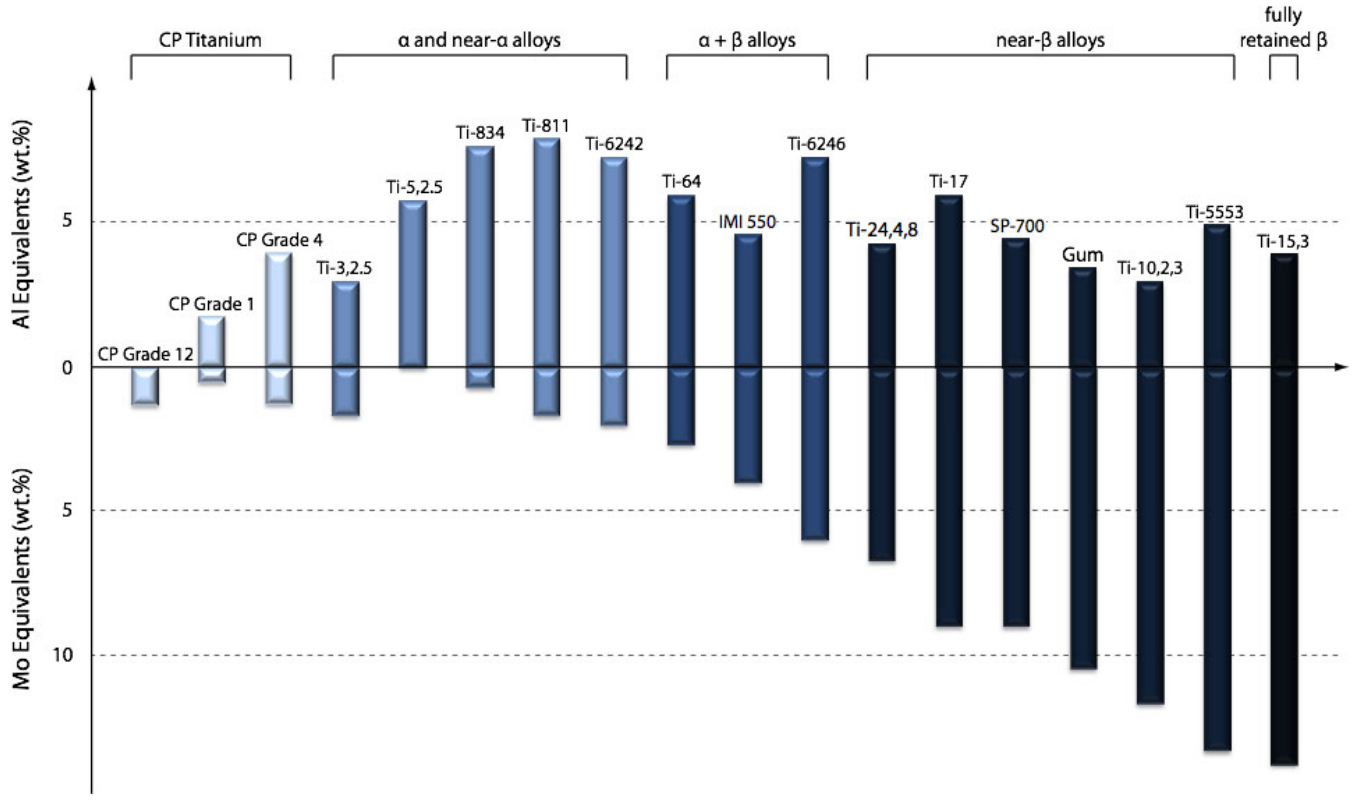

Figure 5: The menagerie of titanium alloys, categorised into classes and showing their $\mathrm{Mo_{eq}}$ and $\mathrm{Al_{eq}}$. From Chapman, Dye research group.

fracture mechanics are valid on when the crack is larger than

$$\frac{1}{\pi}\left(\frac{K_{\mathrm{th}}}{\sigma_{\mathrm{runout}}}\right)^2 = \frac{1}{\pi}\left(\frac{5}{550}\right)^2 = 26\,\mu\mathrm{m} \tag{8}$$

where σ_{runout} is the HCF runout stress. Thus, at threshold a linear elastic analysis cannot even apply (since $1.6 < 26\,\mu\mathrm{m}$). Therefore we are left with measuring the da/dN vs. ΔK curve.

This line of analysis therefore suggests that, for reasonable stresses (near the HCF limit), the size of a threshold crack is so small that non destructive examination cannot possibly be relied upon. Therefore we are forced to rely on having robust manufacturing methods that do not produce defects, as demonstrated ultimately by the testing of large volumes of material (i.e. spin testing).

In addition, this analysis suggests that at threshold the critical crack size will be on the order of the grain size; and so that these materials can initiate cracks from individual microstructural features - they are *microstructure-sensitive*.

In summary then, titanium alloys are strong and tough, but don't work harden much. So once a crack is big enough to grow, it will grow *quickly*. It should be emphasised that there is nothing random about fatigue; cracks grow in an entirely predictable and measurable fashion. Therefore, problems can be avoided, deterministically, by keeping the stress low enough that an plausible defect won't give rise to crack growth. Its only if we insist on going beyond that stress that we need worry about probabilistic defect distributions and crack growth.

7.1. The Alloys; Microstructure-property correlations

We turn now to examine the main titanium alloys; Figure 5 shows a number of major titanium alloys grouped into classes and by their $\mathrm{Mo_{eq}}$ and $\mathrm{Al_{eq}}$. Commerically Pure (CP) titanium is titanium that contains just a small amount of Fe and Si, and is strengthened by oxygen. Grade 1 CP Ti for example, contains 1800 ppmw O (0.18 wt.$) whereas Grade 4 CP Ti contains 4000 ppmw.

Near-α alloys are used in high temperature applications (see next lecture) and contain very little β phase. The leading near-α alloys are Ti-811, Ti-834 and Ti-6242. Therefore they have some α stabilisers but very little β stabiliser. The presence of all the alloying elements means they have an open $\alpha + \beta$ phase field for hot working.

The $\alpha + \beta$ alloys include Ti-6Al-4V, which is the main alloy we have been discussing, and Ti-6246. Ti-6Al-2Sn-4Zr-6Mo have slightly more β phase than Ti-64 and much slower kinetics, owing to the high Mo content. This makes it processing rather easier and make it possible to obtain fine α laths. The α phase is strengthened by Al, Zr, Sn, and O whilst the β is Mo-strengthened.

The near-β or metastable β alloys include landing gear alloys such as Ti-5553 and Ti-10-2-3, as well as some superelastic biomedical alloys. Ti-5553, Ti-15-3 and Ti-10-2-3 can be forged and heat treated to give very high specific strengths.

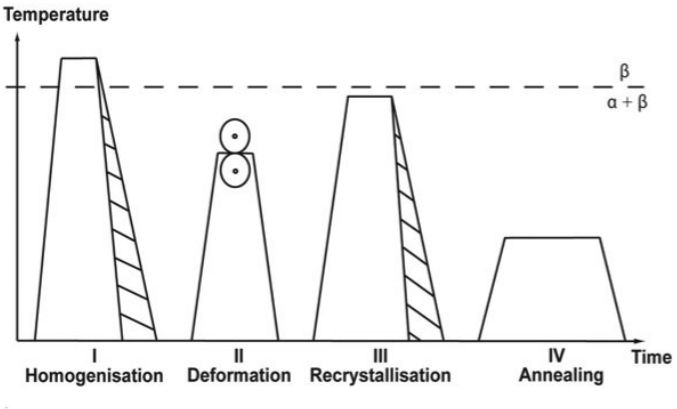

Figure 6: Processing route for bimodal microstructures, schematically. From Lütjering and Williams.

Processing Step (see Fig. 5.6)	Important Parameters	Microstructural Features
I	Cooling Rate	Width of α Lamellae ($\rightarrow \alpha_p$ Size)
II	Deformation Temperature Deformation Degree Deformation Mode	Texture Type – Texture Intensity – Dislocation Density Texture Symmetry
III	Annealing Temperature Cooling Rate	– Vol% of α_p ($\rightarrow$ β Grain Size) – Alloy Element Partitioning Width of α Lamellae
IV	Annealing Temperature	– Ti_3Al in α – Secondary α in β

Table 1: Effect of process variations in stages I-IV on the microstructures that result. From Lütjering and Williams.

Depending on how we process an alloy, we can tailor the microstructure and thereby, the properties. Looking at the first relationship (Table 1), with reference to our bimodal microstructure processing schematic (Figure 6), we observe the following. First, the cooling rate form the β determine the α lath thickness. How we deform these laths affects the crystallographic texture we obtain. Then, the globularisation temperature affects the composition and fraction of the α_p, and the cooling rate the secondary α_s plate width. Any final ageing then affects any final α precipitation from the β, and may produce Ti_3Al α_2.

These features then affects the properties as follows, Table 2. In both lamellar and bimodal structures, making the $'\alpha_p$ or laths smaller improves strength but at the cost of fatigue crack growth behaviour - crack bridging is reduced. Similarly, a bimodal microstructure is stronger that a colony structure, which also results in an improved ΔK_{th} for naturally initiated cracks ("microcracks"), but again at a cost in fatigue crack growth behaviour. Ageing in α_2 does result in more strength, but at a cost in ductility, crack initiation and crack growth and is therefore generally undesirable. In alloys such as Ti-6246, producing very fine secondary α is good for strength with no drawbacks, expect in ductility. Finally, for textured ma-

	$\sigma_{0.2}$	ε_F	HCF	Micro-cracks ΔK_{th}	Macrocracks ΔK_{th} R = 0.7	Macrocracks K_{Ic}	Macrocracks ΔK_{th} R = 0.1	Creep Strength 0.2%
Small α Colonies, α Lamellae [a]	+	+	+	+	–	–	–	+/–
Bi-Modal Structure [b]	+	+	–	+	–	–	–	–
Small α Grain Size [c]	+	+	+	+	–	–	–	–
Aging (α_2), Oxygen	+	–	+	–	–	–	+	+
Secondary α in β	+	–	+	+	0	0	0	+
Texture: Stress ∥ c-Axis	+	0	+ Vac – Air	0 Vac – Air	0 Vac – Air	0	0 Vac – Air	+

[a] Compared to coarse lamellar structure.
[b] Compared to fully lamellar structure with same cooling rate.
[c] Compared to large α grain size of fully equiaxed structures.

Table 2: Correlation of microstructural variables with the observed mechanical behaviour, in $\alpha+\beta$ alloys. From Lütjering and Williams.

terial then putting the tensile stress along the c-axis is detrimental (in air), even though it is stronger.

7.2. Textures in materials

We have been edging our way around the issue of textures, the crystallographic distributions of orientations, since at least when we first looked at anisotropy in MSE203. Since deformation in titanium is so anisotropic, so crystallographic in nature, we now really have to turn to consider how we describe orientation distributions.

Stereographic projections are a way of depicting the location of a point on a surface of a sphere - say the direction of a plane normal - on 2D paper. If we take a point (say O in Figure 7), then draw a line between it an the south pole, we take the point where it passes through the equatorial plane. Then, in Figure 7(b), the stereographic projection is that equatorial plane - so the North and South poles lie at the centre. This projection has the enormous benefit that angles are preserved - circles plot as circles.

Turning to Figure 8, (a) shows the cubic unit cell with its {100}, {110} and {111} planes and their normals shown. The north pole is in the direction of (001), and 0 and 90° longitude are the (100) and (010). If we take all of those plane normals and project them onto the equatorial plane, Figure 8(b), we obtain Figure 8(c). The small triangles described by $\{001\}-\{011\}-\{111\}$ are the minimal symmetrically related units for a cubic crystal. For a hexagonal crystal, the minimum symmetrically related area is a 60° segment of the full stereographic projection, described by $\{0001\}-\{01\bar{1}\bar{0}\}-\{1\bar{2}10\}$.

A popular way to depict crystal orientations is to plot *inverse pole figures*. There, for each location in a microstructure, the crystallographic plane normal (pole) to some sample direction in the sample is found and the fre-

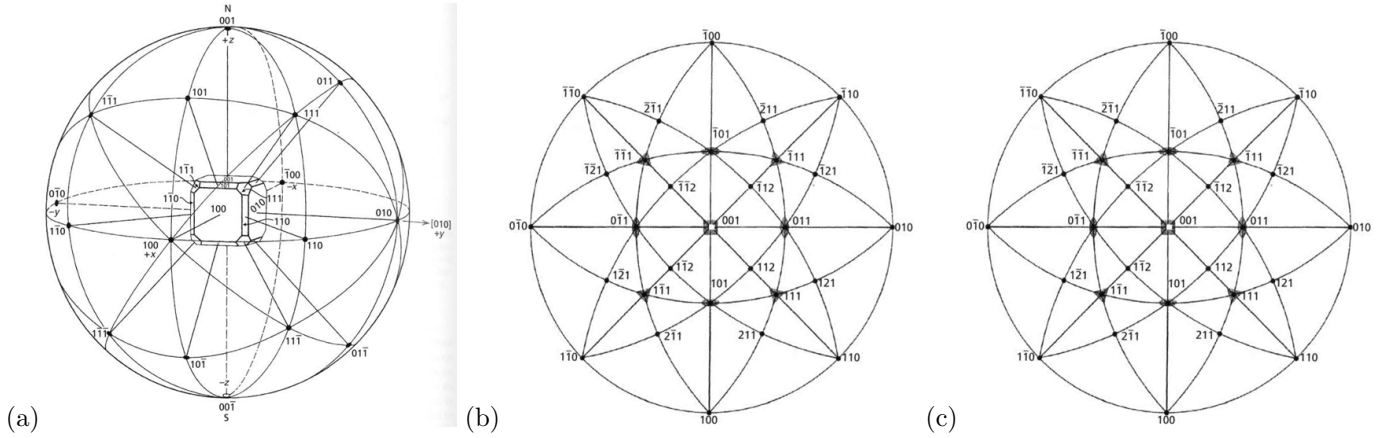

Figure 8: (Construction of an inverse pole figure, for a cubic crystal (a) the cubic unit cell and its major planes, with their normals (poles) projected onto a sphere. (b) Those poles projected onto a stereographic projection. (c) Resulting stereogram, also showing the major symmetry axes. From Hammond.

quency distribution of these poles plotted on the unit stereogram.

Another, more popular way to plot a pole figure corresponds to the way the measurement is performed using X-ray or neutron diffraction. This, the most traditional way to measure texture, works as shown in Figure 9. The sample is placed into an X-ray diffractometer. If a diffraction pattern were to be measured in θ–2θ mode, keeping the sample normal on the bisector of the incident and collected beams, then the patterns at right might be obtained. There, the intensity of some of thee peaks varies not just

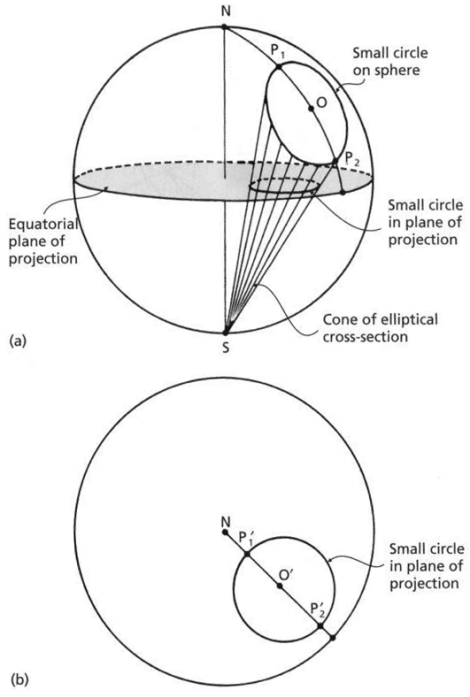

Figure 7: (a) Construction of a stereographic projection by projecting from the surface of a sphere, through the equatorial plane to the south (or north) pole. (b) Depiction of the equatorial plane, which is the stereographic projection. From Hammond

according to the structure factor (and geometric factors from the scattering geometry), but also according to the frequency of occurrence of grains where those particular plane normals are normal to the sample in that orientation. So the Figure shows two patterns for CP Ti bar, along its axis and along its hoop direction - and notice that the {0002} peak is so weak that it is practically absent form the axial measurement.

If we then keep the diffractometer fixed on a particular diffraction peak $\{hkil\}$ - at a particular 2θ setting, and change the orientation of the sample (goniometer angles χ and ϕ in the Figure), we can then plot how the intensity of that $\{hkil\}$ varies with *sample orientation*, in what is called a *pole figure*. In practice, several (3+) pole figures are measured, corrected for experimental factors, and then a complete, consistent orientation distribution is constructed. From this, individual pole figures are then plotted, Figure 9(a). There, the textures for cross-rolled Ti-64 plate are shown.

In fact, a complete orientation distribution requires the variation in frequency with three angles. An example is shown in Figure 10. There are several ways to understand why three angles are required to describe an orientation. First, consider an orientation tensor with three orthogonal right-handed unit basis vectors. Describing the first of these requires knowledge of the first two co-ordinates - the third can be found from unit length. For the second basis vector, it must be normal to the first and of unit length, so only a single number is required to describe it. Then, the third can be found form the cross product of the first two. A second way is to consider an orientation as consisting of knowing the direction of a given pole - say the (0001) *c*-axis - which requires two numbers just iike our first basis vector. Then, a direction perpendicular to that axis can be described by a rotation about it - say the direction of $(11\bar{2}0)$. This is called an axis-angle pair. A third way is to think of a boat on the surface of the Earth. To know everything about the boat we need to know its location -

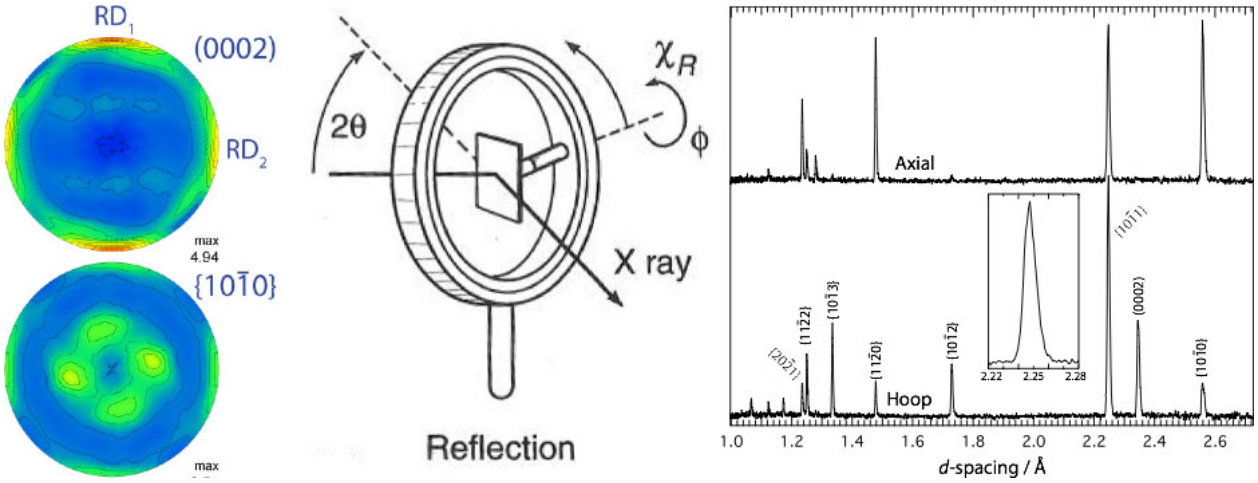

Figure 9: (left) Example of two pole figures, for the {0002} and {10$\bar{1}$0}, measured for cross-rolled Ti-6-4 plate using lab. X-ray diffraction (Warwick, red=most intense, green = 1× random, blue=least intense). (middle) setup of a pole figure measurement on an X-ray diffractometer, from Hammond. (right) diffraction patterns for two directions in CP Ti bar material (Warwick).

latitude and longitude - and its direction - the way it is pointing.

Therefore, a single pole figure can't describe an orientation distribution fully - it only describes the frequency for the particular plane normal measured. Thus, several pole figures are measured and combined mathematically to get the complete orientation distribution. But, for most human purposes it is easier to examine pole figures when we are thinking about textures, because we can readily relate them to directions in crystals.

The Bunge description of orientations uses three Euler angles, Figure 11. The first, ψ_1, describes a rotation about Z, rotating X and Y as shown. Then, we rotate by ϕ about the new (dotted) X-axis, which rotate Z to Z'. The final, third, rotation is also about Z', by an angle ψ_2, to obtain the final X' and Y' axes (leaving Z' alone).

A second way to measure textures is in the SEM. There, if we tilt the sample by 70° to the incident beam and examine the electron scattering at 90° to the incident beam, we observe channelling patterns. These Kikuchi bands, which intersects at poles, correspond to electrons channelling down the planes of the crystal. These bands can be fitted to a model of the crystal structure and the (complete) crystal orientation obtained. We can then find the direction of the crystallographic plane normal to a particular sample direction - the location in the inverse pole figure (IPF) - and assign a colour according to that IPF. Then , we can plot the spatial variation in these colours, obtaining an 'orientation-coloured microstructural map,' Figure 12. Often, the IPF is with respect to the sample

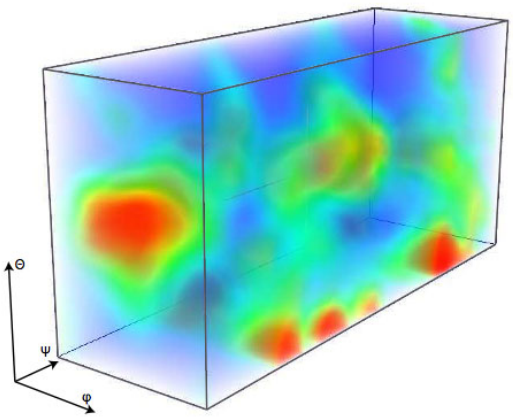

Figure 10: Example of a complete orientation distribution function (ODF), in β annealed Ti-6Al-4V plate (Warwick). A pole figure only shows frequency vs two angles, whereas the full ODF requires three angles, produced by combining 3 or more pole figures.

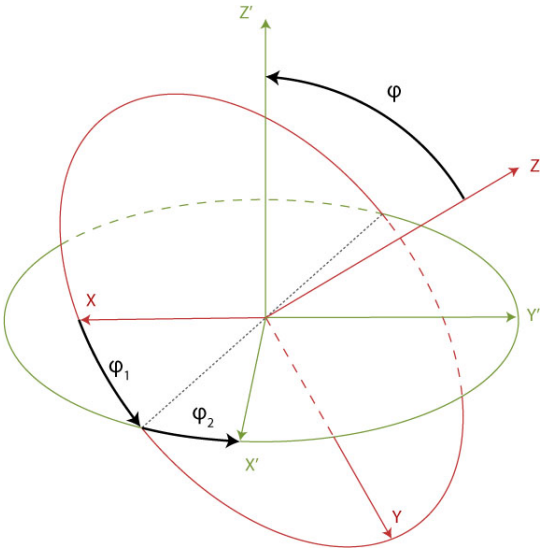

Figure 11: Rotation of a set of orthonormal basis vectors (XYZ, red) by a set of Bunge Euler angles (ψ_1 about Z, then ϕ about X, then ψ_2 about Z') to a new orientation. From Warwick, PhD thesis, Imperial College, 2012.

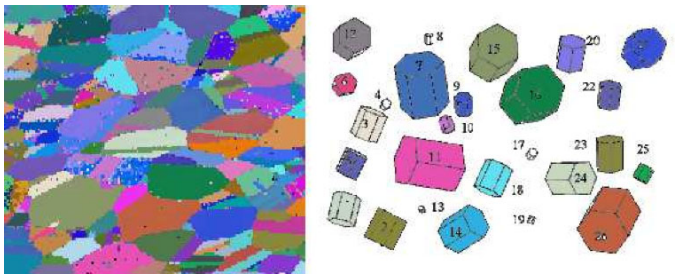

Figure 12: Example of an EBSD map, coloured according to orientation. The individual colour orientations are depicted on the hexagonal prisms at right.

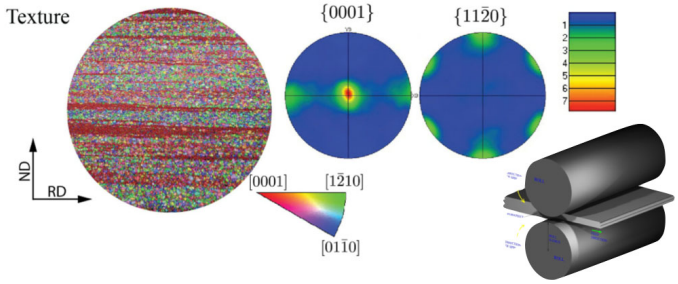

Figure 13: Example of a unidirectionally rolled plate texture (Peter Tympel, Dye research group, 2015), with the EBSD map at left, coloured according to the IPF shown. The rolling directions are also shown.

normal in the SEM, but this can be changed in software. Often, adjacent to this we will plot some pole figures to get an idea of the overall orientation distribution.

An example is provided in Figure 13, which shows the texture for unidirectionally rolled Ti-64 plate. In rolling, we term the long direction of the plate - the direction of feed - the rolling direction (RD). The normal to the plane of the plate is termed the normal direction (ND). Finally, the third orthogonal direction is termed the transverse direction (TD). Importantly, notice that the plate thins in the ND and extends in the RD, but that this is a state of plane strain - the TD stays the same with zero strain in that direction.. This is because the plate is much wider than it is thick, so it can't spread (much). Cross- rolling is where the plate is rotated by 90° between rolling passes, so that there are two Rolling directions and no TD. Unidirectional rolling is where the plate is rolled in the same orientation in every pass.

In the texture shown, this particular bimodal / nearly equiaxed Ti-6Al-4V product form is found to have extensive macrozones, corresponding to the flattened prior-β grains (even though it was probably rolled in the $\alpha + \beta$ regime). Some, corresponding to most of the grains, has their basal planes in the TD. This is because in metal forming, rotation during slip occurs so that the soft direction ends up in the straining direction. So the hardest direction ends up in the undeformed direction, the TD. The remaining macrozones are composed of grains with their {0002} in the RD.

A third way to measure a texture is using X-ray synchrotron diffraction, Figure **??**. There, a very high energy X-ray beam is used that can penetrate the sample completely, leading to the production of diffraction rings on an area detector placed beyond the sample. Typically, X-ray energies around 60-100 keV are used, which equate to wavelengths in the region of 0.15 Å. The diffraction angles 2θ are therefore quite small - on the order of 5°. Then, the 3 and 9 O'clock positions in the diffraction ring correspond to the loading direction, for example, and the 12 O$\mathbb{O}$position to a direction normal to the sample axis. Thus, the variation in intensity around the ring corresponds the variation in the frequency of plane normals that correspond to the outer ring of the corresponding pole figure. But, because many diffraction peaks can be captured simultaneously, it is possible to mathematically reconstruct the complete orientation distribution.

The advantage of this is that it can be done very fast, in situ whilst changing the sample due to some condition like straining or heating. Routinely, it can be done in ms and the fastest I have ever measured data from an area detector was in ~ 100 ps. In contrast, Lab. X-ray textures take on the order of 4 h to measure, and EBSD textures are around 100 patterns per second - meaning that measuring a statistically representative sample of grains (say a thousand) will also take several hours. Most commonly today, however, EBSD has taken over from lab X-ray sources for measuring textures - the analysis is more direct and spatial variations can be examined.

A comparison of the three techniques is shown in Figure 15, for cross-rolled Ti-6Al-4V plate. Again, the {0002} are found in the two transverse (rolling) directions. The EBSD map shows slightly more variability, which isn't found by the X-ray measurement because it measures a larger area. The reconstruction from the EBSD data has given an artefact at the centre of the pole figure (which was reconstructive, not measured), but in general the three are in reasonable agreement.

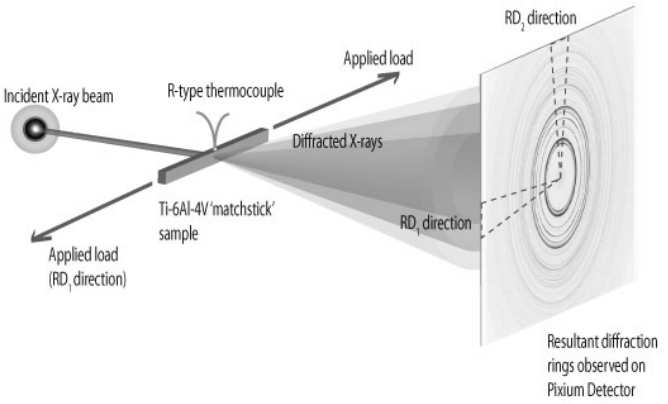

Figure 14: Experimental setup for transmission measurements of texture evolution in situ using monochromatic synchrotron X-rays with an area detector. From Warwick et al, Dye research group, 2012.

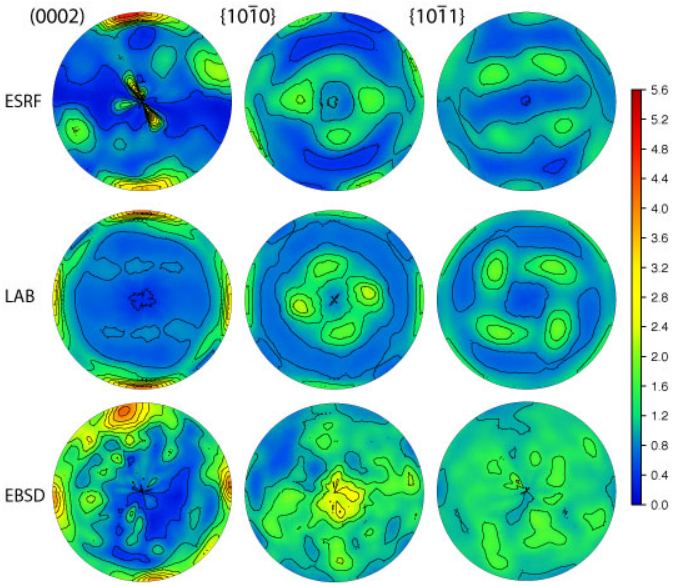

Figure 15: Comparison of textures measured in the same cross-rolled Ti-6Al-4V plate by the three different techniques. From Warwick et al, Dye research group, 2012.

Know we know how to measure and interpret textures, turn now to examine the differences in texture between different product forms of Ti-6Al-4V, Figure 16. We have already examined the UD rolled texture (middle). Cross-rolled product shows a softer overall texture, with the stronger {0002} in the TD of the final rolling pass, and the other {0002} in the TD of the preceding, alternating, pass. The bar form was produced by rolling bar/ingot material continuously. Therefore it has a fairly, but not completely, circularly symmetric texture, with the soft {10$\bar{1}$0} in the bar long direction (ED). Notice also that the bar texture is less intense.

Turning now to the consequences of texture, Figure 17 provides data for the un-notched stress-life curves for uni-directionally rolled material loaded parallel and transverse to RD, where the predominant /0002/ texture direction is therefore in the TD. It is found that loading along the hard {0002} direction (transverse) gives rise to lower fa-

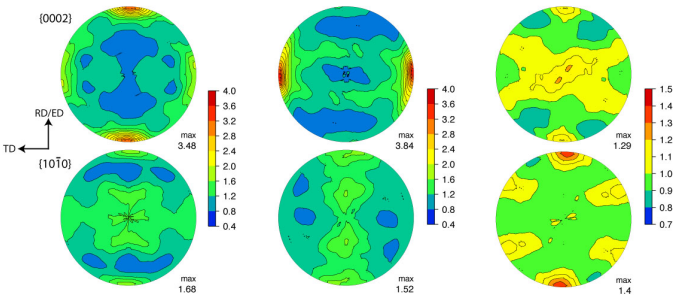

Figure 16: Textures in Ti-6Al-4V in cross rolled (left), undirectionally rolled (middle) and bar (right) product forms. All showed bimodal microstructures that were quite similar in appearance in optical microscopy. From Warwick et al, Dye research grip, 2012.

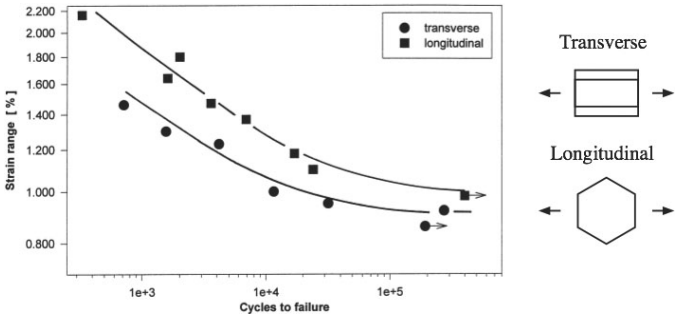

Figure 17: Effect of texture on the S-N behaviour for Ti-6-4. From Lütjering and Wiliams.

tigue strengths, whilst loading along the easy slip directions produces higher fatigue strengths. On one level this is unsurprising - loading along the c-axis produces a brittle response. But we turn now to investigate fatigue further.

7.3. Micromechanisms of fatigue

We have already discussed the slip behaviour of α/β colony structures and the crystallography of slip in Ti in general, in lecture 5. We found that one prism slip direction was easy, another was hard, and the third prism slip system was in the habit plane and therefore very difficult, and so that colony structures would be very anisotropic. In general, Ti doesn't work harden much and so localisation of slip is easy - and in particular is promoted by hydrogen and α_2. Slip localisation may also be promoted by oxygen. We have also introduced the elastic anisotropy of α-Ti. We turn now to think about how these processes will result in fatigue, in an attempt to link the dislocation mechanisms to the measured macroscopic behaviour. It should be emphasised that this is an ongoing area of research, where our thinking is still changing.

The classical picture of fatigue initiation, e.g. in pure Cu single crystals deformed in HCF for millions of cycles, starts with considering a source slip band. In each cycle, it slips back and forth, extruding and pultruding slip steps. These result in a step at the sample surface, as shown in Figure 18. These steps give rise to a stress concentration, which intimates a notch that becomes a crack.

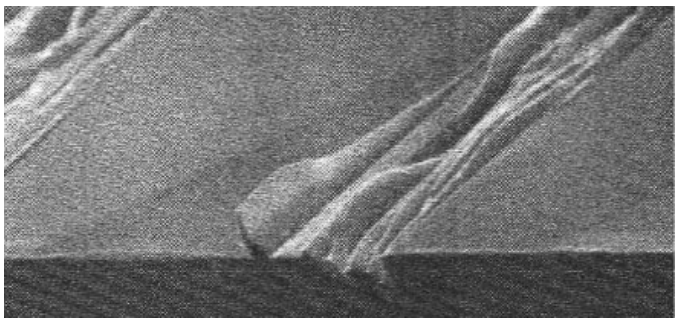

Figure 18: Cu single crystal cycled in HCF showing intrusion and extrusion on the sample surface.

Cold dwell fatigue is a particular phenomenon of interest in the titanium industry. In this phenomenon, 10× reductions in cyclic life are observed when a load hold of several minutes is introduced at the peak load during a fatigue cycle at ambient temperature.

Today, the leading concept for subsurface dwell fatigue crack initiation comes from a modified Stroh pile-up model. In this depiction, a source slip band in a soft grain that is blocked by the grain boundary results in a large applied shear stress at the head of the slip band in an adjacent hard-oriented grain, with its {0002} plane normal near the loading direction. This grain is then sheared open on or near its {0002} plane, via a mechanism yet to be determined, producing a facetted {0002} plane on the initiating grain. This model agrees with most of the observations observed in dwell fatigue cracking when large volumes of material, like discs, are tested.

There is some empirical support for this picture, from crystal plasticity finite element models by both Dunne and by Ghosh. They looked at the longitudinal stress variation across a soft-hard-soft grain combination model. The stress in the middle of the grain varies between the soft and hard grains because of their different stiffnesses - because the {0002} grain is stiffer, at a given load then the requirement for strain continuity means that the load is higher. But also, and especially once plastic relaxation has been allowed to occur, then there is a stress peak at the grain boundary. That is, plasticity leads to the generation of additional grain boundary accommodation stresses between the two grains.

Now, we need to return to our da/dN curve and re-examine the significant of different per-cycle crack growth rates, Figure 21. If Δa is less than one lattice spacing (a few Å) per cycle, we are definitely in a regime where continuum mechanics cannot apply. And for titanium alloys, this is the position for near-threshold (short) fatigue cracks. Once we get into the situation where the crack grows 10 + nm per cycle, we are probably safely into a continuum regime, until at final failure we get into static, cup-and-cone type ductile failure mechanisms. This should be borne in mind when the following evidence is examined.

We turn now to examine some real experimental fatigue fracture surfaces. Bantounas examined Ti-6Al-4V under high-R HCF situations. He found that some macrozones had striations, and some had facets. Figure 22. Pilchak has recently determined that facets grow far faster than striations, which are a ductile, Paris-law regime fatigue mode. The initiation region was also a region that pro-

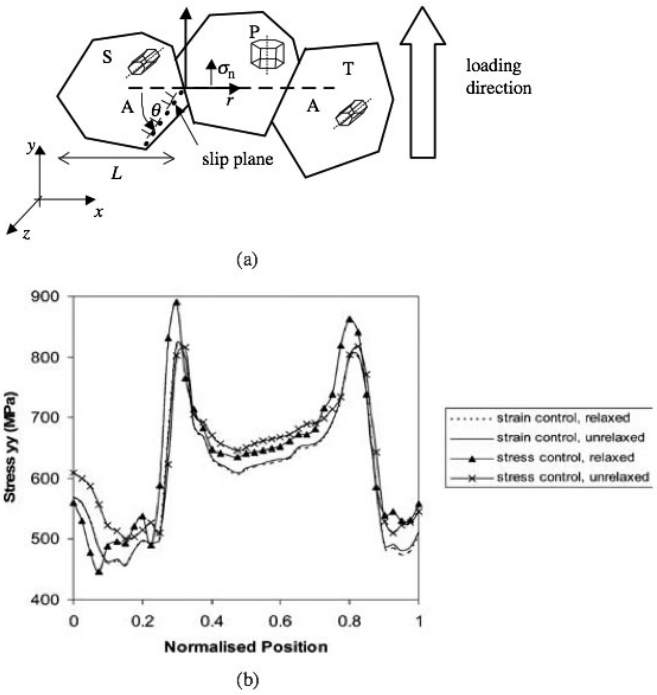

Figure 20: Crystal Plasticity Finite Element (CPFE) model of load relaxation on load cycling a model soft-hard-soft grain combination in α-Ti. From Dunne.

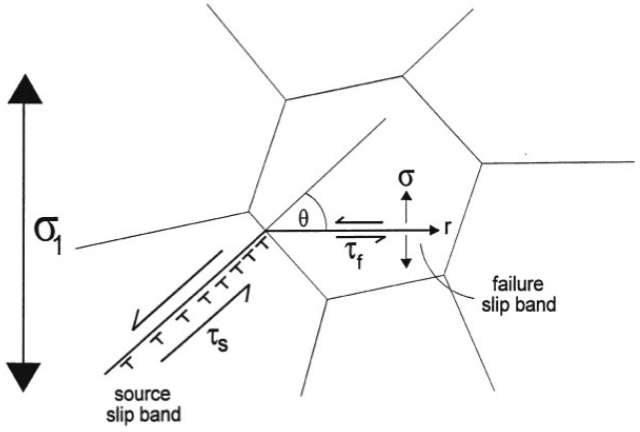

Figure 19: Depiction of the modified Stroh model for cold dwell fatigue fracture initiation. From Dunne.

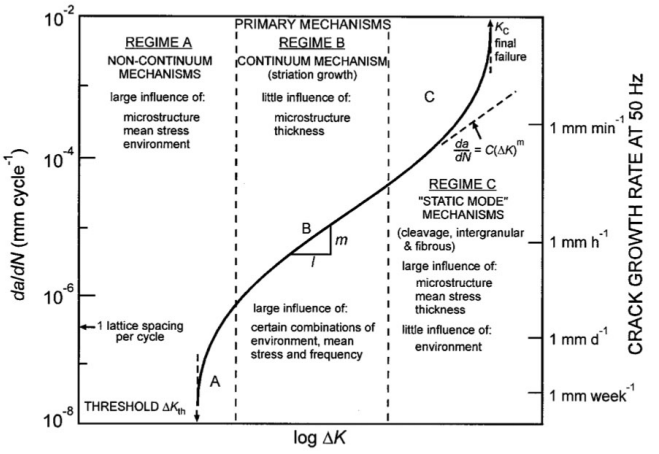

Figure 21: Division of a fatigue crack growth curve into regions corresponding to different cracking mechanisms. From Ritchie.

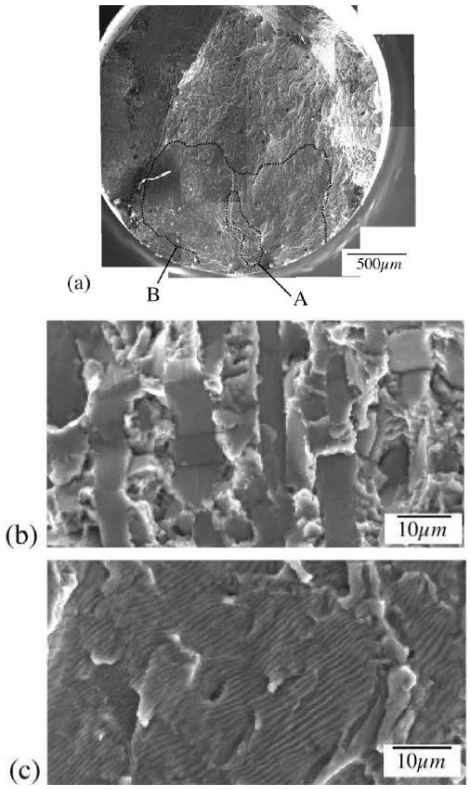

Figure 22: High-R HCF fatigue fracture surface in plate Ti-6Al-4V. Some regions show a faceted fatigue cracking mode, which were also the initiating region. Others showed a striated cracking mode. From Bantounas et al, Dye research group, 2010.

duced facetted cracking features.

It should be pointed out that Pilchak has shown that the facets formed at low ΔK, near-threshold, are not features that form over a single fatigue cycle. He grew fatigue cracks in lamellar Ti-64 where 10 cycles of overload were used in between alternately 200, 400 and 600 cycles of regular LCF. The 10 cycle overloads produced macroscopic beachmarks that were striated (regular Paris law regime). The longer intervals were smooth and facetted, but corresponded to multiple fatigue cycles and their length wasn't due to the microstructure (e.g. a primary α grain) but corresponded to the number of fatigue cycles. So it was concluded that the facets were smooth and featureless and grew incrementally, slowly in every fatigue cycle.

Returning to Bantounas' work, he found that in his case (high-R HCF in testpieces) the facets were inclined 20-50° with respect to the loading axis, and had a near-{0002} normal. In contrast, the striated regions were either not inclined, or highly inclined, and were mostly not near-{0002}. When the fracture surfaces were sectioned, the facetted regions could be correlated with macrozones with their {0002} near the loading direction, whilst the striated regions had their {0002} far from the loading direction.

It was concluded that facetting was associated with {0002} macrozones loaded near to the loading direction,

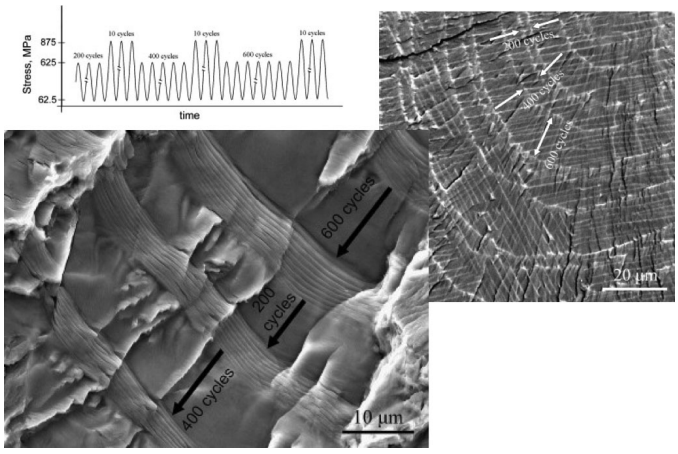

Figure 23: Variable amplitude loading in TI-6-4, showing through the use of overloads and different intervals that the low stress facetted fatigue crack growth mode is incremental; facets do not grow in a single cycle, at least in that example. From Pilchak et al, 2009.

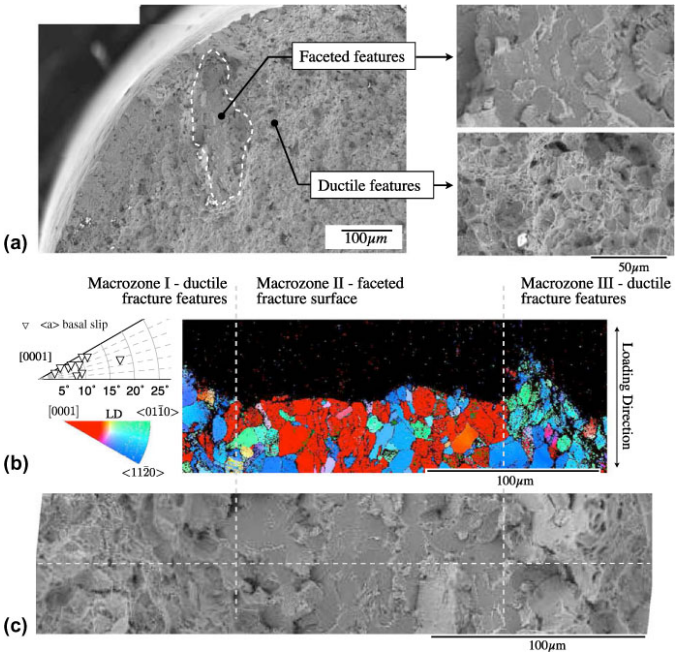

Figure 24: Relationship of facetted regions in Figure 22 and striated regions to the underlying macrozones and their orientation. From Bantounas et al, Dye research group, 2010.

but importantly that these were inclined such that there was an applied shear stress. When the Schmid factors were examined, it was found that the facetted grains were poorly oriented for both $<c+a>$ and $<a>$-slip.

The motivation for Bantounas' study was to understand why bar Ti-64 showed better high-R HCF performance than UD, which was better than cross-rolled. The conclusion was that the order in performance correlated with the fraction of {0002} orientations inclined in the critical declination for basal facetting to occur.

It should be noted that this phenomenology is different to that presented for cold dwell fatigue earlier. There,

the dwell facets usually have their plane normal along the loading direction, whilst for high-R HCF they are inclined. But, in both cases the facets are smooth and near-{0002}. Clearly, a key part of texture engineering titanium is to avoid having {0002} plane normals in vulnerable directions that result in facetting.

7.4. Summary

We have started to examine mechanical properties of titanium alloys, starting with the stress-strain curves and then looking at both S-N and fatigue crack growth curves. We have met the alloys and classified them into groups. Then, we have discussed textures, and that has lead us into the beginnings of a discussion about fatigue micromechanisms, which we will pick up in the next lecture.

Thus far, we have noted that the fatigue in a very crystallographic way, with the macrozones observed translating into the fracture surfaces we see. We have also seen that facet formation is an important part of the phenomenology, that these are usually near-{0002} and that they are not $N = 1$ features. We have also begun to think about how such facets might form.

— END OF LECTURE —